

**Topological phonon-magnon hybrid excitations in a two-dimensional honeycomb ferromagnet**Han Huang  and Zhiting Tian <sup>\*</sup>*Sibley School of Mechanical and Aerospace Engineering, Cornell University, New York 14853, USA*

(Received 23 November 2020; revised 23 July 2021; accepted 27 July 2021; published 11 August 2021)

We develop a phonon-magnon interaction model for the two-dimensional honeycomb ferromagnet and calculate the band structure of the hybrid phonon-magnon excitation. When the phonon (either acoustic or optical) energy overlaps with the magnon energy, the degeneracies at the crossing points are lifted by the phonon-magnon interaction, leading to topological band inversion. We show that the Berry curvatures and Chern numbers are nonzero around the phonon-magnon band-crossing areas but vanish throughout the rest of the Brillouin zone. We calculate the thermal Hall conductance enabled by the phonon-magnon interaction, which is also an indicator of nontrivial topological properties. In addition, we show that band topologies can be manipulated by varying spin-exchange coupling strengths and Dzyaloshinskii-Moriya interactions strengths.

DOI: [10.1103/PhysRevB.104.064305](https://doi.org/10.1103/PhysRevB.104.064305)**I. INTRODUCTION**

Interactions between basic energy carriers in a condensed system have been among the most well-studied problems and cast significant impacts. Specifically, two types of heat carriers, phonons [1–4] and magnons [5–8], have been long studied separately but seldom considered together since their interaction is usually too small to be physically important. Nevertheless, the phonon-magnon interaction started attracting attention recently because of interesting phenomena arising from their interaction, such as broadening of the Raman spectrum [9] and phonon/magnon softening [10,11]. Meanwhile, the discovery of topological insulators has stimulated the venture of searching for other types of condensed-matter systems with topological behaviors, such as the topological band structure of phonons and magnons.

The earliest consideration of phonon-magnon interaction can be dated to the Kittel theory, which predicted phonon attenuation at simultaneous resonance [12,13]. Further insights were given in the Callen-Callen theory of magnetostriction, which, although only considered the global strain on the lattice, extended the spin-lattice interaction to more complicated lattices by point-group symmetry considerations [14,15]. More recently, a more general theory employing quantum field treatments for  $\text{Cs}_2\text{CuCl}_4$  was given by Kreisel *et al.* [16], in which the magnetic-field dependence of elastic constants and the ultrasonic attenuation rate were studied. The hybrid magnon-phonon modes in  $h\text{-YMnO}_3$  were experimentally observed using inelastic neutron scattering [17]. In addition, the theory of phonon-magnon interaction by long-range dipole-dipole interaction (DDI) and without sublattice structure was proposed by Takahashi and Nagaosa [18], and short-range phonon-magnon interaction was studied for a simple ferromagnetic square lattice [1,19]. On the other hand, the topological nature of phonon Hall effects in a honeycomb dielectric with Raman spin-phonon coupling was also reported [20].

Dzyaloshinskii-Moriya interactions (DMI) were found to introduce the topological properties and the thermal Hall effect of magnon systems [5–7]. Simple ferromagnetic square-lattice systems with phonon-magnon interaction were also predicted to exhibit nontrivial Berry curvature [1,19]. However, such overly simplified models are unlikely to capture important details of the interaction, such as the effects of more complicated lattice symmetry. Therefore, it is desired to use a more realistic structure, such as honeycomb lattice, to demonstrate the topological properties caused by phonon-magnon interaction. One of the major distinctions between the honeycomb ferromagnets and square ferromagnets is that the square lattice has the edge-shared lattice geometry, which cancels with the  $U(1)$  gauge field and forbids the existence of the DMI-induced nontrivial Berry connection [2,21]. Thus, the honeycomb lattice not only provides a multiband magnon model but also opens possibilities for a richer space of phonon-magnon interaction with more complicated lattice symmetry.

In this paper, we develop a model for the two-dimensional (2D) honeycomb ferromagnet with explicit couplings between phonons and magnons. We consider a hybrid phonon-magnon system since they are both bosons, and when the energy scales of lattice vibration and spin wave are close, it is more reasonable to treat them on an equal footing. Because the honeycomb lattice has two atoms per unit cell, it embodies both acoustic and optical phonons. We include the interactions between the magnons and both types of phonons, which are different from the previous lattice models using a single atom per unit cell. We consider a model with short-range spin-lattice coupling, which is different from the models involving DDI. Then we numerically calculate the hybrid phonon-magnon spectra. The band inversion is observed, implying the nontrivial topological properties of the system. This demonstrates that the short-range coupling can give rise to topological behaviors in 2D honeycomb ferromagnet. We deduce from the symmetry-breaking perspective that the phonon-magnon interaction enables the thermal Hall effect, indicating nontrivial topological properties. To further show the topological

<sup>\*</sup>zhiting@cornell.edu

behavior of the hybrid phonon-magnon system, we calculate the Berry curvatures and Chern numbers for the hybrid phonon-magnon bands, as well as the thermal Hall conductance. By varying magnon exchange and phonon-magnon coupling parameters, we show that the band topology can be altered by tuning those parameters. Our honeycomb ferromagnetic system closely resembles the newly experimentally realized 2D ferromagnetic materials (e.g., single-layer CrI<sub>3</sub>), which offers insights in understanding their fundamental mechanisms and future applications, such as spintronics.

## II. MODEL

Consider the hybrid phonon-magnon bosonic Hamiltonian,  $H$ , defined for a 2D honeycomb lattice

$$H = H_{\text{ph}} + H_{\text{mag}} + H_{\text{pm}}, \quad (1)$$

where  $H_{\text{ph}}$ ,  $H_{\text{mag}}$ , and  $H_{\text{pm}}$  are Hamiltonians for phonons, magnons, and the phonon-magnon coupling subsystems, respectively. To model the hybrid honeycomb phonon-magnon system, we expect the matrix form of this Hamiltonian to be represented by an  $8 \times 8$  matrix, in which the first two diagonal terms are the magnon dispersions (labeled by  $\sigma = 1, 2$  corresponding to the two atoms in the honeycomb lattice), and the remaining six diagonal terms represent the phonon dispersions (labeled by  $s = 1, \dots, 6$ ). The  $2 \times 6$  and  $6 \times 2$  rectangular off-diagonal blocks represent the phonon-magnon coupling. Our strategy is to consider the phonon, magnon, and phonon-magnon parts separately, and then combine them into the total  $8 \times 8$  matrix.

The phonon Hamiltonian,  $H_{\text{ph}}$ , is given by the lattice dynamics, and up to the fourth-nearest neighbor is considered. The general equation of motion is given by

$$M_i \ddot{u}_i = \sum_j K^{(ij)} (u_j - u_i), \quad (i = 1, \dots, N), \quad (2)$$

where  $M$  is the mass,  $u_i$  is the displacement from the equilibrium position of the  $i$ th lattice site,  $K^{(ij)}$  is the force-constant tensor capturing the two in-plane and one out-of-plane degrees of freedom of the lattice vibrations, and  $N = 2$  for the honeycomb lattice. By plugging in the force constants and diagonalizing the dynamical matrix associated with the equation of motion, we can obtain the phonon dispersion relations. Here, we use the force constants for 2D graphene for numerical calculations because the CrI<sub>3</sub> lattice involves two Cr atoms and six I atoms per unit cell, which is hard to model theoretically and adds unnecessary complications [22]. We see later that the graphene honeycomb lattice with the fourth-nearest neighbor phonon force-constant tensor is sufficient to capture the topological features of the phonon-magnon band structure successfully (Fig. 1). Finally, we can rewrite the phonon Hamiltonian in terms of creation and annihilation operators

$$H_{\text{ph}} = \sum_{k,s} w_{k,s} \left( a_{k,s}^\dagger a_{k,s} + \frac{1}{2} \right), \quad (3)$$

where  $w_{k,s}$  is the phonon frequency of phonon mode with momentum  $\mathbf{k}$  in branch  $s$ ; and  $a_{k,s}^\dagger$  and  $a_{k,s}$  are phonon creation and annihilation operators. Here we consider both acoustic

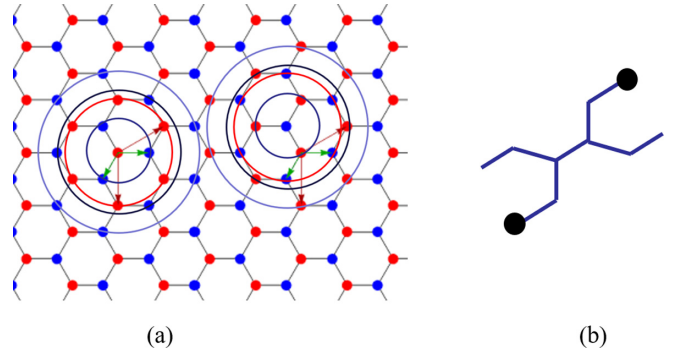


FIG. 1. (a) The fourth-nearest neighbors of two sublattices highlighted using concentric circles; (b) The “twist” vibration of the two highlighted atoms need to be modeled using the fourth-nearest neighbor.

and optical phonons. Because the energy of flexural optical phonon (ZO) phonon branch in graphene overlaps with the acoustic branches, we should pay special attention to it. The ground-state energy can be ignored for now. Later in the numerical calculation, we add a negligible on-site potential to avoid the singularity caused by the zero  $\Gamma$ -point phonon energies of the acoustic branches, which appear in the denominator of the phonon-magnon coupling elements.

To obtain the XY ferromagnetic magnon Hamiltonian with  $x$ -axis quantization,  $H_{\text{mag}}$ , we start with the spin Hamiltonian,  $H_{\text{spin}}$  [5], and only consider the first-nearest exchange coupling for simplicity,

$$H_{\text{spin}} = -2J \sum_{\langle ij \rangle} (S_i^x S_j^x + S_i^y S_j^y) + D \sum_{\langle\langle ij \rangle\rangle} v_{ij} (S_i^y S_j^z + S_i^z S_j^y), \quad (4)$$

where the nearest exchange couplings  $J$  and the second-nearest in-plane DMI ( $\mathbf{D} = D \hat{x}$ ) are considered, and  $v_{ij} = \pm 1$  for opposite hopping directions. Here, the single and double angle brackets represent the first and second-nearest sites, respectively;  $S_i^x$  and  $S_i^y$  are  $x$  and  $y$  component of the spin operators for the specified magnetic ion, respectively. For magnetic ions with large spin (e.g., spin 3/2 for Cr<sup>3+</sup> in CrI<sub>3</sub>), we can use the linear Holstein-Primakoff (HP) transformation to obtain a good approximation. For  $x$ -axis quantization, we write  $S_i^y$  and  $S_i^z$  in terms of the magnon creation and annihilation operators  $S_i^\pm = S_i^y \pm iS_i^z$ ,  $S_i^+ = \sqrt{2S}b_i$  and  $S_i^- = \sqrt{2S}b_i^\dagger$  by only keeping the lowest (linear) order term. We introduce a structure factor,

$$g(\mathbf{k}) = \frac{1}{3} \sum_l e^{i\mathbf{k} \cdot \mathbf{r}_l}, \quad (5)$$

where  $\mathbf{r}_l$  donates the spatial coordinate for the three-nearest neighboring sites ( $l = 1, \dots, 3$ ). Then the eigenfrequencies of the XY ferromagnetic can be solved by diagonalizing a non-Hermitian Bogoliubov Hamiltonian [5],

$$\omega_{\mathbf{k},\sigma} = \left[ \left( 3v_s \pm \sqrt{(v_D \rho_{\mathbf{k}})^2 + \left( \frac{3v_s |\mathbf{g}\mathbf{k}|}{2} \right)^2} \right)^2 - \left( \frac{3v_s |\mathbf{g}\mathbf{k}|}{2} \right)^2 \right], \quad (6)$$

where  $v_s = JS$ ,  $v_D = DS$ , and  $\rho_k = \sum_l \sin(\mathbf{k} \cdot \boldsymbol{\rho}_l)$ , where  $\boldsymbol{\rho}_l$  donates the spatial coordinate for the second-nearest neighboring sites ( $l = 1, \dots, 6$ ). We properly scale the nearest exchange-coupling constant and DMI strength constants such that the magnon energies are close to the acoustic phonon energy range so that we can investigate the band structure at the phonon and magnon band-crossing points [6].

Next, we obtain the phonon-magnon coupling Hamiltonian. The general form of the spin-lattice coupling term is given by [17]

$$H_{sl} = - \sum_i \sum_{\Gamma} B^{\Gamma} \sum_i \epsilon_i^{\Gamma} S_i^{\Gamma}(i), \quad (7)$$

where  $\Gamma$  labels different irreducible representations of the hexagonal point group,  $B^{\Gamma}$  is the symmetrized phonon-magnon coupling constant associated with  $\Gamma$ ,  $\epsilon_i^{\Gamma}$  is the symmetrized strain, and  $S_i^{\Gamma}$  is the symmetrized products of spin operators, with  $S_i^{\Gamma} = \{(S_i^z)^2 - 1/3 S(S+1), (S_i^x)^2 - (S_i^y)^2, 1/2(S_i^x S_i^y + S_i^y S_i^x), 1/2(S_i^y S_i^z + S_i^z S_i^y), 1/2(S_i^x S_i^z + S_i^z S_i^x)\}$ , and  $(S_i^x)^2 + (S_i^y)^2 + (S_i^z)^2 = S(S+1)$ . Hence,  $H_{sl}$  can be further simplified into a linear form,

$$H_{sl} = - \sum_i S_i^T E_i S_i, \quad (8)$$

where the spin operators  $S_i = (S_i^x, S_i^y, S_i^z)^T$  can be directly rewritten in terms of linearized HP magnon operators. The coupling matrix  $E_i$  is written in terms of the Cartesian strain tensor

$$\epsilon_{\alpha\beta}^i = \frac{1}{2}(E_{\alpha\beta} + E_{\beta\alpha}) = \frac{1}{2} \left( \frac{\partial u_i^{\beta}}{\partial r_{\alpha}} + \frac{\partial u_i^{\alpha}}{\partial r_{\beta}} \right), \quad (9)$$

where  $u_i^{\alpha}$  is the  $\alpha$ th component of the displacement of the lattice site  $i$  and  $r_{\alpha}$  is the  $\alpha$ th component of its location. We

can expand  $\mathbf{u}_i = \mathbf{u}(\mathbf{r}_i)$  in the phonon coordinates

$$\mathbf{u}(\mathbf{r}_i) = \sum_{k,s} \boldsymbol{\xi}_{k,s} \sqrt{\frac{1}{2Mw_{k,s}}} (a_{k,s} + a_{-k,s}^{\dagger}) e^{ik \cdot \mathbf{r}_i}, \quad (10)$$

where  $\boldsymbol{\xi}_{k,s}$  is the phonon polarization vector. We can rewrite the two-ion strain tensor in the limit of small displacement for numerical calculations [23]

$$\epsilon_{\alpha\beta}^{ij} = \frac{1}{2} [(r_{i\alpha} - r_{j\alpha})(u_{i\beta} - u_{j\beta}) + (r_{i\beta} - r_{j\beta})(u_{i\alpha} - u_{j\alpha})], \quad (11)$$

where  $r_{i\alpha}$  is the  $\alpha$ th component of the location of the atom at the  $i$ th lattice site. The relative displacement is given by averaging over the strains from nearest-neighboring ions

$$\tilde{\epsilon}_{\alpha\beta}^i = \frac{1}{N} \sum_j \epsilon_{\alpha\beta}^{ij}. \quad (12)$$

Our goal is to write the Hamiltonian in terms of phonon and magnon creation and annihilation operators to couple them together. We need first to symmetrize the strain tensor to reduce the coupling matrix for the hexagonal honeycomb lattice. From the Callen-Callen theory [15] of magnetostriction, we can write down the point-group symmetrized local coupling matrix with a set of four spin-lattice coupling constants  $B_{12}^{\alpha}$ ,  $B_{22}^{\alpha}$ ,  $B^{\gamma}$ , and  $B^{\epsilon}$  associated with the fully symmetrical representations, which are essential for modeling the complicated couplings between various types of lattice distortions and spin degrees of freedom in the realistic honeycomb lattice. Since we choose the quantization axis to be the  $x$  axis, the contribution of  $B_{12}^{\alpha}$  and  $B_{22}^{\alpha}$  vanishes by the symmetry construction.

We generalize the Callen-Callen theory into local strains for each lattice site  $i$  [17]

$$E^i = \begin{pmatrix} B_{12}^{\alpha} \epsilon^{\alpha,1} - \frac{B_{22}^{\alpha}}{2\sqrt{3}} \epsilon^{\alpha,2} & & \frac{B^{\gamma}}{2} \epsilon_2^{\gamma} & & \frac{B^{\epsilon}}{2} \epsilon_2^{\epsilon} \\ & \frac{B^{\gamma}}{2} \epsilon_2^{\gamma} & & B_{12}^{\alpha} \epsilon^{\alpha,1} - \frac{B_{22}^{\alpha}}{2\sqrt{3}} \epsilon^{\alpha,2} - \frac{B^{\gamma}}{2} \epsilon_1^{\gamma} & & \frac{B^{\epsilon}}{2} \epsilon_1^{\epsilon} \\ & & \frac{B^{\epsilon}}{2} \epsilon_2^{\epsilon} & & \frac{B^{\epsilon}}{2} \epsilon_1^{\epsilon} & \\ & & & & & B_{12}^{\alpha} \epsilon^{\alpha,1} + \frac{B_{22}^{\alpha}}{2\sqrt{3}} \epsilon^{\alpha,2} + \frac{B^{\gamma}}{2} \epsilon_1^{\gamma} \end{pmatrix}, \quad (13)$$

where  $\epsilon^{\alpha,1} = \epsilon_{xx} + \epsilon_{yy} + \epsilon_{zz}$ ,  $\epsilon^{\alpha,2} = (\sqrt{3}/2)(\epsilon_{zz} - \frac{1}{3}\epsilon^{\alpha,1})$ ,  $\epsilon_1^{\gamma} = \frac{1}{2}(\epsilon_{xx} - \epsilon_{yy})$ ,  $\epsilon_2^{\gamma} = \epsilon_{xy}$ ,  $\epsilon_1^{\epsilon} = \epsilon_{yz}$ , and  $\epsilon_2^{\epsilon} = \epsilon_{xz}$  are the symmetrized strains according to the representations of the hexagonal point group. We rewrite the coupling matrix  $E_i$  in terms of phonon operators and do the Fourier transform; then we can absorb all the constants into one, given as

$$E_{\sigma,k}^{\alpha\beta} = \sum_s (a_{k,s} + a_{k,s}^{\dagger}) G_{k,s,\sigma}, \quad (14)$$

where  $G_{k,s,\sigma}$  is the matrix containing the spin-lattice coupling constants and can be added together with the independent phonon and magnon Hamiltonians to form the total bosonic Hamiltonian. Once the spin-lattice Hamiltonian is completely rewritten using the phonon and magnon bosonic operators, we can convert the spin-lattice Hamiltonian  $H_{sl}$  into the phonon-magnon operator,  $H_{pm}$ .

$H_{sl}$  [Eq. (8)] is nondiagonalizable since its components consist of three bosonic operators (two magnon operators and one phonon operator). To solve the hybrid phonon-magnon system, we need to assume that the phonon-magnon interaction is weak to make  $H_{sl}$  [Eq. (8)] diagonalizable. Under the weak coupling assumption, the particle number is conserved, so we can simply drop one of the magnon operators and now  $H_{sl}$  only consists of two bosonic operators, either  $a_k^{\dagger} b_k$  or  $b_k^{\dagger} a_k$ , and hence diagonalizable. The total Hamiltonian can then be approximately written as

$$H \simeq \sum_{\mathbf{k}} \psi_{\mathbf{k}}^{\dagger} \mathcal{H} \psi_{\mathbf{k}}, \quad (15)$$

where  $\psi_{\mathbf{k}} = (c_{\mathbf{k},1}, \dots, c_{\mathbf{k},8})^T$ ,  $\mathcal{H}$  is the  $8 \times 8$  dynamical matrix consisting of all the phonon, magnon, and the coupling information, whose terms are already obtained above, and  $c_{\mathbf{k},\Sigma}^{\dagger}$  and  $c_{\mathbf{k},\Sigma}$  ( $\Sigma = 1, \dots, 8$ ) are the creation and annihilation

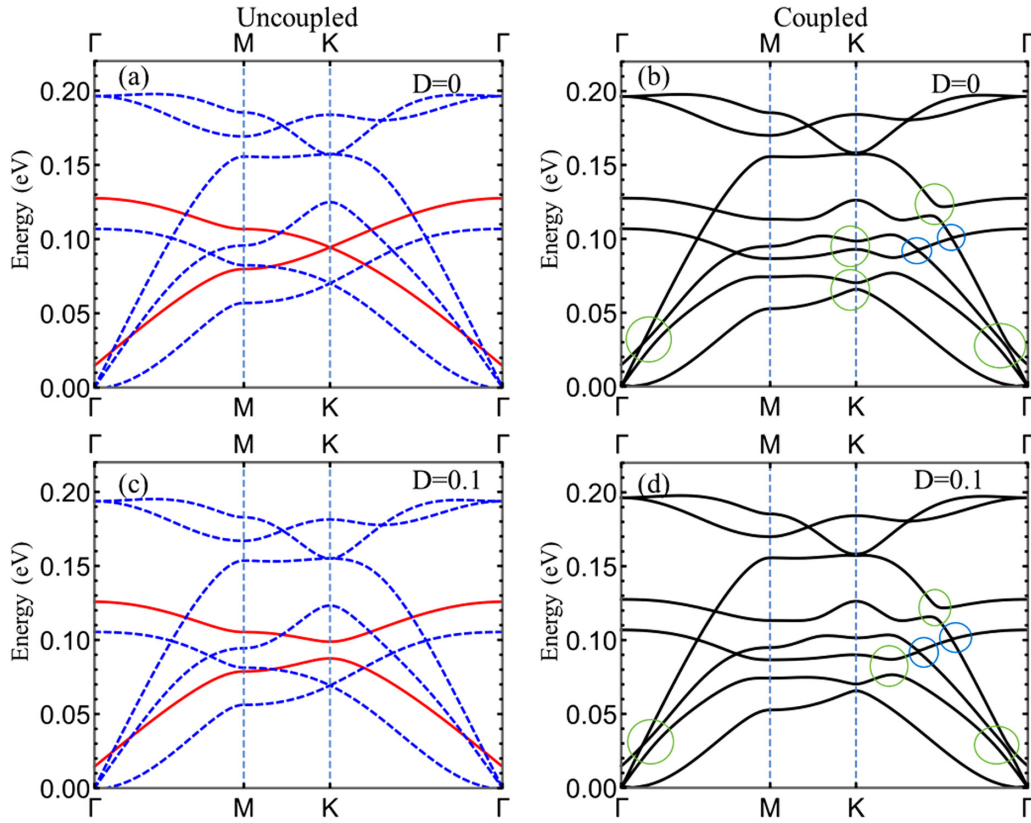


FIG. 2. (a), (c) Uncoupled phonon and magnon modes, with or without DMI, respectively; the blue dashed lines are acoustic phonon branches, and the red solid lines are magnon branches; (b), (d) Coupled phonon and magnon modes, (b) without DMI and (d) with DMI included, clear band inversions can be seen at crossing points, indicating the topological nature of the hybrid phonon-magnon excitation. The band gaps in the blue circles in (b) and (d) are small but exist. Also note that in the  $\Gamma$ - $M$  regime there is a band-gap opening between the originally TA and magnon bands, but not between LA and magnon bands. Here, we use  $B^y = 15$ ,  $B^z = 15$ ,  $J = 1.21$ , and  $D = 0$  in (c), (b), and  $D = 0.1$  in (c), (d).

operators for the hybrid system. The diagonal terms are given by the six phonon and two magnon dispersion relations. The off-diagonal terms are given in terms of  $G_{k,s,\sigma}$ , with  $G_{k,s,\sigma}$  transformed into  $A$  and  $B$  in terms of local coordinates

$$A_{s,\sigma} = \mathbf{a}^{-T} G_{s,\sigma} \mathbf{a}^3, \quad (16)$$

$$B_{\sigma,s} = (A^\dagger)_{s,\sigma}, \quad (17)$$

where  $\mathbf{a}^3 = (1, 0, 0)$ ,  $\mathbf{a}^- = (0, 1, -i)$  for the  $x$ -axis quantization. Note that  $A$  is a  $2 \times 6$  matrix and  $B$  is a  $6 \times 2$  matrix filling the off-diagonal positions of  $\mathcal{H}$ , so that the system is now in a diagonalizable form.

In this representation, the spin-lattice coupling matrix in Eq. (8) can be rewritten in a form that represents the coupling between the coupling between the  $s$  phonon branch and the  $\sigma$  magnon branch at different  $\mathbf{k}$ 's. The total dynamical matrix is then given by

$$\mathcal{H} = \begin{pmatrix} \Omega & A \\ B & W \end{pmatrix}, \quad (18)$$

where  $\Omega = \text{diag}(\{\omega_{k,\sigma}\})$  and  $W = \text{diag}(\{w_{k,s}\})$  are matrices with diagonal elements giving the magnon and phonon dispersion relations. By diagonalizing this matrix, we can obtain the dispersion relations for the hybrid phonon-magnon excitation.

### III. RESULTS AND DISCUSSION

Because the phonon-magnon model is an  $8 \times 8$  matrix with complicated diagonal (fourth-nearest neighbor honeycomb phonon dispersions) and off-diagonal terms (phonon-magnon coupling terms with phonon dispersion relations in the denominator), it would be infeasible to diagonalize the matrix analytically. Hence, we numerically diagonalize the matrix to calculate the hybrid phonon-magnon band structure. Setting  $S = 3/2$  and  $M = 1$ , the other constants used are given in the Appendix [22]. Figure 2 shows the comparison between the dispersion curves of uncoupled and coupled phonon-magnon systems. The blue and red curves in Figs. 2(a) and 2(c) are the original phonon branches and magnon branches, respectively. In Figs. 2(b) and 2(d) band gaps emerge along the  $M$ - $K$ - $\Gamma$  directions. Clearly, there is a band inversion at the crossing points. The off-diagonal phonon-magnon coupling terms in the dynamical matrix open the band gap, similarly as the off-diagonal terms in the Kernel matrix representing the spin-orbit coupling SOC opens the band gap in the topological insulators. Along the  $\Gamma$ - $M$  direction, although there is a band gap between the originally TA and magnon bands, there are no band gaps opened between LA and magnon bands. Furthermore, when the magnon energies overlap with the optical phonon energies, there are also couplings between magnons

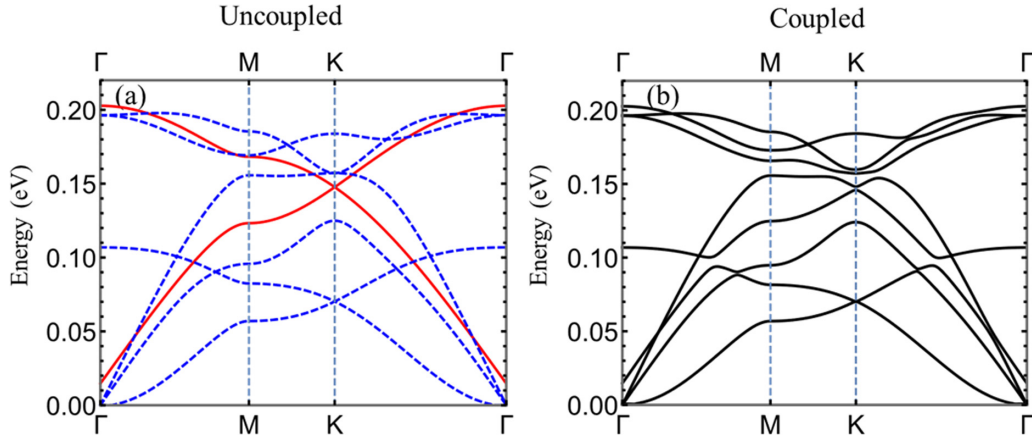


FIG. 3. (a) Uncoupled phonon and magnon branches for the parameters  $J = 2.01$ ,  $D = 0.3$ ,  $B^y = 10$ , and  $B^z = 10$ . (b) Coupled phonon and magnon branches where the upper magnon branch intersects with LO and TO phonons, causing them to gain nonzero Berry curvature and nontrivial topology, as shown in Figs. 6(a) and 6(b).

and optical phonons, resulting in band-gap openings in the  $\Gamma$ - $K$ - $M$  directions, as shown in Fig. 3.

We numerically calculate the Berry curvature associated with each band to elucidate the topological nature of the hybrid phonon-magnon system. The Berry curvatures of a 2D crystal are nonzero only in the  $z$  direction, and the  $z$ -direction Berry curvature associated with a given matrix Hamiltonian

$H$  is given as

$$\Omega_{\Sigma}^z(\mathbf{k}) = i \sum_{\Sigma \neq \Sigma'} \frac{x_{\Sigma}^{\dagger} \partial_{k_x} H x_{\Sigma'} x_{\Sigma'}^{\dagger} \partial_{k_y} H x_{\Sigma} - (k_x \leftrightarrow k_y)}{(\lambda_{\Sigma} - \lambda_{\Sigma'})^2}, \quad (19)$$

where  $x_{\Sigma}$  is the  $\Sigma$ th eigenvector of  $H$ ,  $\lambda_{\Sigma}$  is the  $\Sigma$ 's eigenvalue of  $H$ , and the summation is taken over all

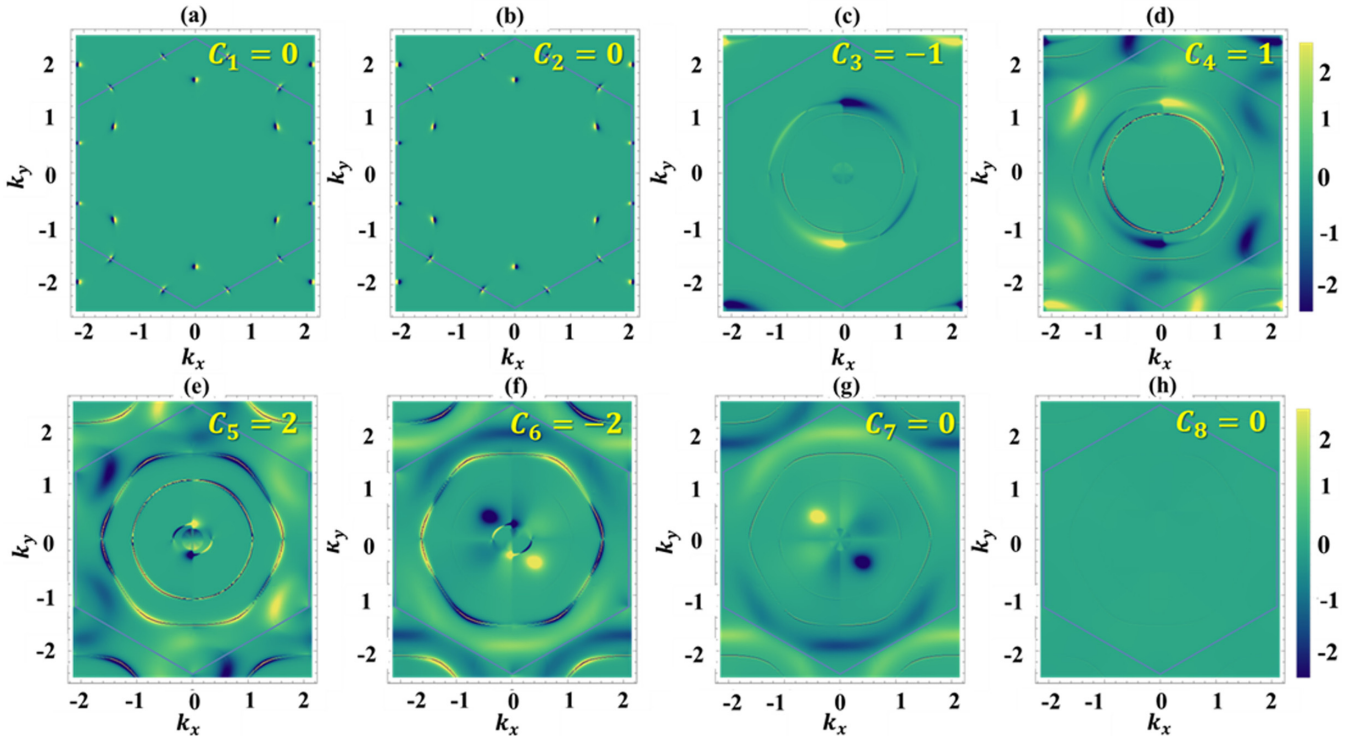


FIG. 4. (a)–(h) The calculated Berry curvature  $\Xi_{\Sigma} = \text{sgn}(\Omega_{\Sigma}^z) \ln(1 + |\Omega_{\Sigma}^z|)$  of the eight phonon-magnon bands (from high to low energies) and their corresponding Chern numbers (labeled on the top-left corners) for a system with  $J = 1.21$ ,  $D = 0$ ,  $B^y = 15$ , and  $B^z = 15$ . The signature of nodal rings from phonon-magnon coupling can be seen in (c)–(g). It is natural to see that the Berry curvatures in (a), (b), and (h) are zero except for the phonon Dirac points.

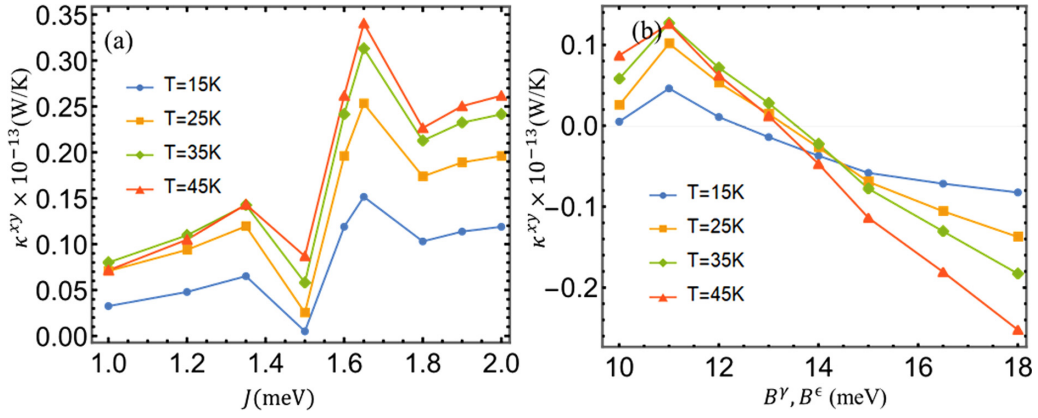


FIG. 5. (a) Thermal Hall conductance plotted versus spin-exchange strength  $J$  at different temperatures. (b) Thermal Hall conductance plotted vs phonon-magnon coupling constants (setting  $B^\gamma = B^\epsilon$ ).

$\Sigma$ 's and  $\Sigma'$ 's, except for  $\Sigma = \Sigma'$ . Normally, for a topologically trivial system, the Berry curvature should be zero everywhere. Figure 4 shows the nonzero Berry curvatures of the system with the phonon-magnon coupling turned on and DMI turned off ( $J = 1.21$ ,  $D = 0$ ,  $B^\gamma = 15$ , and  $B^\epsilon = 15$ ). The Chern number of the energy band is defined as

$$C^\Sigma = \frac{1}{2\pi} \int_{\text{BZ}} dk_x dk_y \Omega_\Sigma^z(\mathbf{k}). \quad (20)$$

For numerical calculation, we adopt the algorithm introduced in Ref. [24] so that the  $k$ -point summation can be performed in a computationally efficient manner. The results are shown in Fig. 4.

It is noteworthy that, besides the phonon-magnon crossing nodal rings, the phonon-phonon crossing points also become Dirac points because of the global time-reversal and spin-rotation ( $\mathcal{T}C_x$ ) symmetry breaking by coupling with the magnons. Neither the phonon part nor the magnon part independently exhibits nonzero thermal Hall currents when DMI is turned off. But, the  $\mathcal{T}C_x$  symmetry breaking causes the

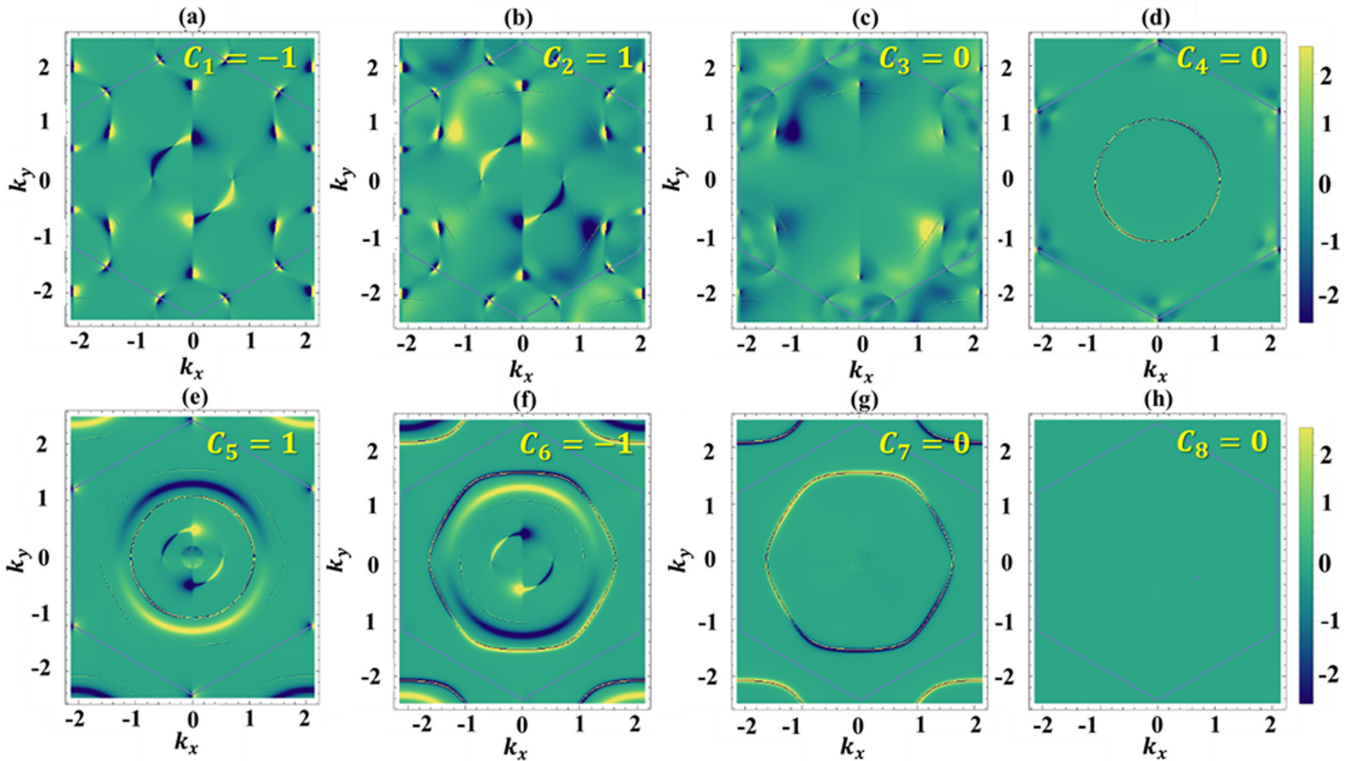


FIG. 6. (a)–(h) The calculated Berry curvature  $\Xi_\Sigma = \text{sgn}(\Omega_\Sigma^z) \ln(1 + |\Omega_\Sigma^z|)$  for the eight phonon-magnon bands (from high to low energies) and their corresponding Chern numbers (labeled on the top-left corners) with  $J = 2.01$ ,  $D = 0.3$ ,  $B^\gamma = 10$ , and  $B^\epsilon = 10$ . We can see in (a) and (b) that as long as the upper magnon band reaches high enough energy to intersect with the optical phonons (TO and LO), the optical branches can also gain nonzero Berry curvature and hence nontrivial topology.

thermal Hall effect. The thermal Hall current is given by

$$\mathbf{j} = \kappa^{\alpha\beta} \hat{\mathbf{z}} \times \nabla T, \quad (21)$$

where  $\kappa^{\alpha\beta}$  is the thermal Hall conductance.

The system's ferromagnetic ordering breaks the time-reversal ( $\mathcal{T}$ ) symmetry, but when combined with the spin-rotation ( $\mathcal{C}_x$ ) operation, the system with neither phonon-magnon interaction nor DMI preserves  $\mathcal{TC}_x$  symmetry [19]. Under the  $\mathcal{TC}_x$  operation,  $\mathbf{j} \rightarrow -\mathbf{j}$  while  $\nabla T$  is invariant. So, if the system preserves  $\mathcal{TC}_x$  symmetry,  $\mathbf{j} = -\mathbf{j} = 0$  so that the thermal Hall conductance,  $\kappa^{\alpha\beta}$ , must be zero. However, the spin-lattice Hamiltonian breaks the  $\mathcal{TC}_x$  symmetry by coupling the spin operators with an extra  $\frac{\partial u}{\partial r} \sim \mathbf{k}u$ -dependent term obtained from the spatial derivative in the strain tensor, lifting the  $\mathcal{TC}_x$  symmetry constraint cast on  $\mathbf{j}$  and makes it possible to be nonzero. The thermal Hall conductance can be written in terms of the Berry curvature [1,25–27]

$$\kappa^{xy} = -\frac{k_B^2 T}{\hbar V} \sum_{n,\mathbf{k}} c_2(f_{n,\mathbf{k}}) \Omega_{\Sigma}^z(\mathbf{k}), \quad (22)$$

where  $f_{n,\mathbf{k}} = 1/\exp(\frac{\hbar\lambda_{\Sigma}(\mathbf{k})}{k_B T}) - 1$  is the Bose-Einstein distribution function,  $k_B$  is the Boltzmann constant,  $T$  is the temperature,  $V$  the volume of the sample, and

$$c_2(f_{n,\mathbf{k}}) = (1 + f_{n,\mathbf{k}}) \ln^2 \frac{1 + f_{n,\mathbf{k}}}{f_{n,\mathbf{k}}} - \ln^2 f_{n,\mathbf{k}} - 2 \text{Li}_2(-f_{n,\mathbf{k}}), \quad (23)$$

where  $\text{Li}_2(z)$  is the polylogarithm function. We set  $T = 15, 25, 35,$  and  $45$  K, and  $B^y = B^e$  for simplicity, and plot the parameter ( $J, B^y,$  and  $B^e$ ) dependence of  $\kappa^{xy}$  to show the nontrivial topology caused by the broken  $\mathcal{TC}_x$  symmetry, as shown in Fig. 5. The scale of  $\kappa^{xy}$  agrees with the previous result reported for the square ferromagnet system [19].

By tuning the parameters of the magnon part, we can study the effects of the parameter dependence of the band topologies. We use a different set of spin-correlation strength and coupling constants ( $J = 2.01, D = 0.3, B^y = 10,$  and  $B^e = 10$ ), and as shown in Figs. 3(a) and 3(b), the band structure is clearly different, with new band gaps appearing within the LO and TO phonon regime, as well as different band gaps in the acoustic and ZO phonon regime. In this parameter setting, when the upper magnon energy is high enough to cross with the optical phonons, the highest two branches which are

TABLE I. Phonon force constants used in the model Ref. [22].

$\phi_r(1)$	36.5	$\phi_r(3)$	3
$\phi_{ii}(1)$	24.5	$\phi_{ii}(3)$	-5.25
$\phi_{io}(1)$	9.82	$\phi_{io}(3)$	0.15
$\phi_r(2)$	8.80	$\phi_r(4)$	-1.92
$\phi_{ii}(2)$	-3.23	$\phi_{ii}(4)$	2.29
$\phi_{io}(2)$	-0.4	$\phi_{io}(4)$	-0.58

originally TO and LO phonons can also gain nonzero Berry curvature, Chern numbers, and hence nontrivial topology, as shown in Figs. 6(a) and 6(b).

#### IV. CONCLUSION

In this work, we develop a general phonon-magnon interaction formalism for the 2D honeycomb ferromagnet by treating those two types of excitations as hybrid phonon-magnon excitations. We calculate the dispersion curves by numerically diagonalizing the hybrid dynamical matrix and deduce from the band inversions at the crossing points that the system has topological properties. Furthermore, we calculate the Berry curvatures and associated them with each hybrid phonon-magnon band. We also compute the thermal Hall conductance to show the topological nature of the system. We show that the thermal Hall conductance can be affected by the spin-exchange and phonon-magnon coupling parameters. We provide a realistic model sufficient for modeling the phonon-magnon systems in the context of honeycomb lattice, and our result demonstrates nontrivial topological properties in such systems. The topological nature of phonon-magnon excitations can be useful in caloritronics [28] and magnonics [29] applications.

#### ACKNOWLEDGMENT

The authors acknowledge Cornell startup funding.

#### APPENDIX

All constants used in the model are listed in Table I. The phonon force constants are extracted from graphene and up to fourth-nearest neighbor. The spin-exchange strength, DM strength, and the phonon-magnon coupling constants are chosen such that the features of the result are made clear.

[1] G. Go, S. K. Kim, and K. J. Lee, Topological Magnon-Phonon Hybrid Excitations in Two-Dimensional Ferromagnets with Tunable Chern Numbers, *Phys. Rev. Lett.* **123**, 237207 (2019).  
 [2] H. Katsura, N. Nagaosa, and P. A. Lee, Theory of the Thermal Hall Effect in Quantum Magnets, *Phys. Rev. Lett.* **104**, 066403 (2010).  
 [3] J. Li, L. Wang, J. Liu, R. Li, Z. Zhang, and X.-Q. Chen, Topological phonons in graphene, *Phys. Rev. B* **101**, 081403(R) (2020).

[4] X. Li, B. Fauqué, Z. Zhu, and K. Behnia, Phonon Thermal Hall Effect in Strontium Titanate, *Phys. Rev. Lett.* **124**, 105901 (2020).  
 [5] S. A. Owerre, A first theoretical realization of honeycomb topological magnon insulator, *J. Phys.: Condens. Matter* **28**, 386001 (2016).  
 [6] L. Chen, J.-H. Chung, B. Gao, T. Chen, M. B. Stone, A. I. Kolesnikov, Q. Huang, and P. Dai, Topological Spin Excitations in Honeycomb Ferromagnet CrI<sub>3</sub>, *Phys. Rev. X* **8**, 041028 (2018).

- [7] S. A. Owerre, Topological magnon bands and unconventional thermal Hall effect on the frustrated honeycomb and bilayer triangular lattice, *J. Phys.: Condens. Matter* **29**, 385801 (2017).
- [8] R. Hidalgo-Sacoto, R. I. Gonzalez, E. E. Vogel, S. Allende, J. D. Mella, C. Cardenas, R. E. Troncoso, and F. Munoz, Magnon valley hall effect in CrI<sub>3</sub>-based van der Waals heterostructures, *Phys. Rev. B* **101**, 205425 (2020).
- [9] A. De Andrés, J. L. Martínez, and P. Odier, Dynamical study of the structural and magnetic phases in Pr<sub>2</sub>NiO<sub>4</sub> single crystals by Raman spectroscopy, *Phys. Rev. B* **45**, 12821 (1992).
- [10] P. Knoll, C. Thomsen, M. Cardona, and P. Murugaraj, Temperature-dependent lifetime of spin excitations in RBa<sub>2</sub>Cu<sub>3</sub>O<sub>6</sub> ( $R = \text{Eu, Y}$ ), *Phys. Rev. B* **42**, 4842 (1990).
- [11] X. B. Wang, J. X. Li, Q. Jiang, Z. H. Zhang, and D. C. Tian, Spin-phonon renormalization of the excitation energy in a dilute two-dimensional antiferromagnet, *Phys. Rev. B* **50**, 7056 (1994).
- [12] L. W. McKeenan, Physical theory of ferromagnetic domains, *Phys. Rev.* **79**, 745 (1950).
- [13] C. Kittel, Interaction of spin waves and ultrasonic waves in ferromagnetic crystals, *Phys. Rev.* **110**, 836 (1958).
- [14] E. R. Callen and H. B. Callen, Static magnetoelastic coupling in cubic crystals, *Phys. Rev.* **130**, 2600 (1963).
- [15] E. Callen and H. B. Callen, Magnetostriction, forced magnetostriction, and anomalous thermal expansion in ferromagnets, *Phys. Rev.* **139**, A455 (1965).
- [16] A. Kreisel, P. Kopietz, P. T. Cong, B. Wolf, and M. Lang, Elastic constants and ultrasonic attenuation in the cone state of the frustrated antiferromagnet Cs<sub>2</sub>CuCl<sub>4</sub>, *Phys. Rev. B* **84**, 024414 (2011).
- [17] S. L. Holm, A. Kreisel, T. K. Schäffer, A. Bakke, M. Bertelsen, U. B. Hansen, M. Retuerto, J. Larsen, D. Prabhakaran, P. P. Deen, Z. Yamani, J. O. Birk, U. Stuhr, C. Niedermayer, A. L. Fennell, B. M. Andersen, and K. Lefmann, Magnetic ground state and magnon-phonon interaction in multiferroic  $h$ -YMnO<sub>3</sub>, *Phys. Rev. B* **97**, 134304 (2018).
- [18] R. Takahashi and N. Nagaosa, Berry Curvature in Magnon-Phonon Hybrid Systems, *Phys. Rev. Lett.* **117**, 217205 (2016).
- [19] X. Zhang, Y. Zhang, S. Okamoto, and D. Xiao, Thermal Hall Effect Induced by Magnon-Phonon Interactions, *Phys. Rev. Lett.* **123**, 167202 (2019).
- [20] L. Zhang, J. Ren, J.-S. Wang, and B. Li, Topological Nature of the Phonon Hall Effect, *Phys. Rev. Lett.* **105**, 225901 (2010).
- [21] T. Ideue, Y. Onose, H. Katsura, Y. Shiomi, S. Ishiwata, N. Nagaosa, and Y. Tokura, Effect of lattice geometry on magnon Hall effect in ferromagnetic insulators, *Phys. Rev. B* **85**, 134411 (2012).
- [22] R. A. Jishi, L. Venkataraman, M. S. Dresselhaus, and G. Dresselhaus, Phonon modes in carbon nanotubes, *Chem. Phys. Lett.* **209**, 77 (1993).
- [23] W. E. Evenson and S. H. Liu, Theory of magnetic ordering in the heavy rare earths, *Phys. Rev.* **178**, 783 (1969).
- [24] T. Fukui, Y. Hatsugai, and H. Suzuki, Chern numbers in discretized Brillouin zone: Efficient method of computing (spin) Hall conductances, *J. Phys. Soc. Jpn.* **74**, 1674 (2005).
- [25] X.-L. Qi, T.-L. Hughes, and S.-C. Zhang, Topological field theory of time-reversal invariant insulators, *Phys. Rev. B* **78**, 195424 (2008).
- [26] X.-L. Qi, Y.-S. Wu, and S.-C. Zhang, Topological quantization of the spin hall effect in two-dimensional paramagnetic semiconductors, *Phys. Rev. B* **74**, 085308 (2006).
- [27] G. E. Volovik, An analog of the quantum Hall effect in a superfluid <sup>3</sup>He film, *Sov. Phys. JETP* **67**, 1804 (1988).
- [28] G. E. W. Bauer, E. Saitoh, and B. J. Van Wees, Spin caloritronics, *Nat. Mater.* **11**, 391 (2012).
- [29] V. V. Kruglyak, S. O. Demokritov, and D. Grundler, Magnonics, *J. Phys. D: Appl. Phys.* **43**, 264001 (2010).